PH022

Inverse Design and Optimization towards a Leaky Integrate-and-Fire Magnonic Neuron

INTRODUCTION

As artificial intelligence (AI) systems continue to scale, they face increasing computational bottlenecks, particularly due to the separation of compute and memory in traditional von Neumann computing systems. The resulting latency and energy overheads in data movement [1] significantly hinder the efficiency of neural network inference, where throughput and energy efficiency are critical [2].

Neuromorphic systems sidestep these problems by co-locating processing and memory, often through hardware elements that natively emulate the behavior of neurons and synapses [3]. While several electronic and memristive technologies have been explored for this purpose, they have not displayed significant advantages over current conventional computing architectures for large-scale simulation and implementing small-scale, independent cognitive agents [4]. This motivates the continued search for alternative physical platforms for neuromorphic hardware.

Magnonics offers a promising alternative for implementing neuromorphic hardware by substituting electrons with magnons, the quanta of spin waves, as information carriers [5]. Because magnons propagate without charge motion, they can transport and process signals in insulators with minimal energy loss from Joule heating [6,7]. Crucially, their wave nature naturally supports interference, superposition, and frequency multiplexing [8], making magnons well-suited for implementing neuronal operations such as signal integration and nonlinear activation.

In this context, magnonic neurons — nanoscale structures that exploit spin-wave dynamics to emulate neuronal behavior — represent a compelling building block for non-von Neumann computing architectures. Such neurons can perform localized computations and support in-memory processing, offering a pathway toward highly compact and energy-efficient neuromorphic processors.

This work presents the design of a Leaky Integrate-and-Fire (LIF) magnonic neuron capable of performing key neuronal operations of integration, thresholding, and activation using nonlinear magnonic components. Device geometry was optimized using inverse design through direct binary search (DBS), enabling targeted control of spin-wave interference. Micromagnetic simulations of the Landau-Lifshitz-Gilbert (LLG) equation indicate that the structures exhibit behaviors consistent with neuronal operations, such as localized energy accumulation and nonlinear response, highlighting the feasibility of spin-wave-based neuromorphic elements and laying the groundwork for future, fully functional designs.

MATERIALS AND METHODS

Neuron Structure

The magnonic neuron, which has a structure inspired by an optical ring resonator, physically implements a Leaky Integrate-and-Fire (LIF) neuronal model [9]. In this framework, the ring resonator serves as the integration node, where spin waves undergo constructive interference and lead to the amplification of internal spin-wave amplitude. The intrinsic magnetic damping and

coupling losses represent the 'leaky' part of the neuron, where energy dissipates if not replenished by sufficient input. The directional coupler acts as the activation function of the magnonic neuron, directing energy away from the output waveguide until sufficient accumulated energy crosses the critical threshold, at which point it 'switches' and energy remains in the output waveguide [10].

However, a ring resonator alone cannot sustain energy build-up indefinitely, since spin waves readily leak into the output waveguide as well as due to coupling and damping losses. Therefore, an optimized design must minimize spin-wave leakage while still enabling sufficient energy accumulation for neuronal activation.

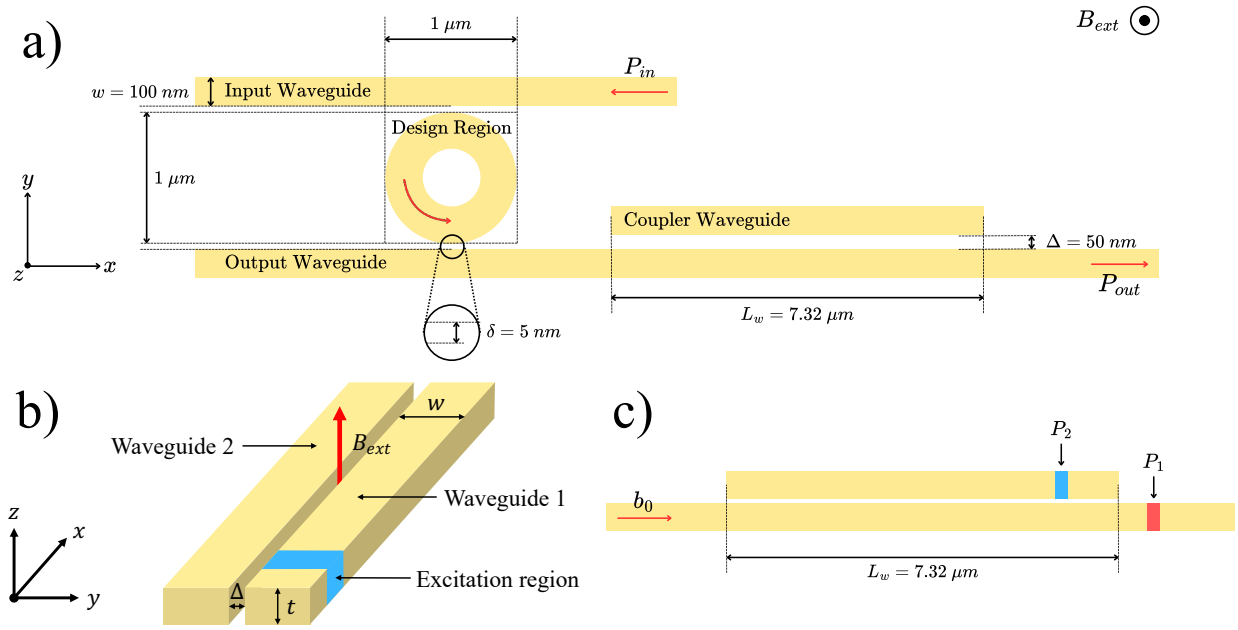

Figure 1. Proposed structures and parameters for inverse-design. *(a) The proposed structure of the inverse-design magnonic neuron. A magnetic field is excited in the input waveguide which travels through the design region and to the output waveguide. The design region, initially a YIG ring with width 150 nm, was set at δ = 5 nm away from the input and output waveguides while the coupler waveguide was set at Δ = 50 nm away from the output waveguide. A 7.32 μm directional coupler was set at 0.58 μm away from the design region to prevent energy transfer. (b) Structure used for determining dispersion curves and mode separation, with waveguide thickness t = 50 nm, width w = 100 nm, and out-of-plane magnetic field B_{ext} = 300 mT. Spin waves were excited over a 40 nm-wide excitation region. (c) Simplified coupler structure to compare spin-wave routing against excitation field strength b_0, with one detector in the coupler away from the damping region and another in the input waveguide after the coupler, away from the damping region.*

Figure 1(a) shows the proposed neuron structure. Micromagnetic simulation was performed using the MuMax^3 micromagnetic package [11] with the following YIG parameters [12]: magnetic saturation $M_s = 1.4 \times 10^5\ A\ m^{-1}$, exchange constant $A = 3.5 \times 10^{-12}\ J\ m^{-1}$ and Gilbert damping $\alpha = 2 \times 10^{-4}$. The Gilbert damping at the ends of the input and output waveguides and the coupler waveguide were exponentially increased to a value of 0.5 to minimize reflections.

Frequency Determination

To design a functional magnonic neuron, it is imperative to know the frequency for optimal energy transfer (i.e., resonance) and how it shifts with power or magnetic field. This allows tuning the geometry, bias field, and input power to achieve desired coupling or decoupling behavior. This desired frequency, known as the resonance frequency, generates spin waves most efficiently [13].

Finding resonant frequencies required plotting transmission *T* as a function of frequency *f*, where *T* is defined by the ratio of the spin-wave intensities in the input waveguide behind and in front of the ring. A sinc pulse was used to excite a broadband signal ranging from 0 GHz to 10 GHz, and a Fast Fourier Transform (FFT) was done at the respective regions to calculate the transmission ratio.

In addition to finding a frequency where the most energy enters the ring, it is also crucial to know the frequency where high amounts of energy enter the output waveguide. Hence, a FFT was also done on the output waveguide under the same excitation, and an FFT magnitude against frequency *f* graph is plotted.

Non-linear Functionality

When parallel identical waveguides are coupled together in proximity, their symmetry ensures that spin wave energy is completely transferred from one to another within a certain distance known as the coupling length [11]. In the proposed magnonic neuron, this directional coupler allows the non-linear switching of spin waves which directly influences its activation behavior.

The coupling length, corresponding to the physical length of the coupler waveguide in Figure 1(c), is given by

$$L_c = \frac{\pi}{|k_s - k_{as}|} = \frac{\pi}{\Delta k} \tag{1}$$

where k_s and k_{as} are the wavenumbers of the symmetric and antisymmetric spin-wave modes respectively. These mode wavenumbers were taken from the spectral map in Figure 3(a), obtained by applying a spatial FFT to the structure in Figure 1(b) under sinc-pulse excitation at 6.7 GHz.

Whether non-linear functionality can take place is dependent by the relative nonlinearity parameter $\eta = |Ta_0^2/4\Omega|$ where T denotes the nonlinear frequency shift coefficient, Ω the coupling efficiency and a_0 the excitation spin wave envelope amplitude, with Ω assumed positive [10]. Nonlinear behavior arises when $\eta > 1$, i.e. $|Ta_0^2| > 4\Omega$.

To ensure stable switching behavior, the group velocities of the symmetric and antisymmetric modes df/dk_s and df/dk_{as} must be approximately equal to eliminate k-dependency (i.e. L_c remains insensitive to changes in input power). This means that waveguide separation δ had to be adjusted such that Ω is reduced and the symmetric and antisymmetric dispersion curves at 6.7 GHz are parallel.

Quantifying spin-wave routing as a function of input power is necessary to determine the activation function of the neuron. Excitation field b_0 was increased incrementally from 3 mT to 60 mT in the structure shown in Figure 1(c) while average power at each waveguide (P_1 and P_2) was taken at the detection regions denoted in red and blue. The final 50% of each simulation timeframe was taken to be averaged to eliminate latency in power due to varying distances from the excitation source.

Direct Binary Search (DBS) Optimization

Using DBS to inverse-design magnonic devices has been described prior in literature [14,15]. In short, a YIG ring geometry was loaded before each cell is flipped (air to YIG and vice versa) in a random order. After each flip, the simulation is run and a reward function determines a score. If the score exceeds the previous score by a certain threshold, the flip is kept and reversed otherwise. Once all the cells are exhausted, a new order is determined and the process is repeated until no further improvements are made, eventually converging to an optimized structure.

However, this method has its own flaws: local minima convergence and the inability to make coarse and fine improvements. We updated DBS to start with larger cell flips (100x100 nm cell size) before cell size decays to 40x40 nm and then 20x20 nm. This allows for coarse improvements at the start, before finer improvements tune the geometry to better support energy buildup.

Other than requiring improvements in output power, properties such as latency [16] (i.e. time-to-fire once sufficient energy has accumulated) and energy efficiency contribute to its overall performance. A simple reward function R was devised that accounts for such factors and improves them during inverse design:

$$R = \int_0^{t_{sim}} P_{out}(t)dt \tag{2}$$

where t_{sim} is the total simulation time and P_{out} the output power measured at the output waveguide before the nonlinear coupler. This specific reward function targets the LIF behavior of the neuron. By maximizing the time-integrated power, the algorithm prioritizes geometries that facilitate constructive interference and rapid energy accumulation, acting as a high-efficiency integration node.

The DBS optimization of the ring resonator was conducted at a field strength of 10 mT. This baseline ensures the system remains within the linear propagation regime, where phase-coherent constructive interference, the physical basis for 'leaking' and 'integrating', is maximized without the interference of nonlinear frequency shifts.

Simulations were run on a workstation with an Intel Core i9-10900 CPU and an NVIDIA GeForce RTX 3070 GPU.

RESULTS

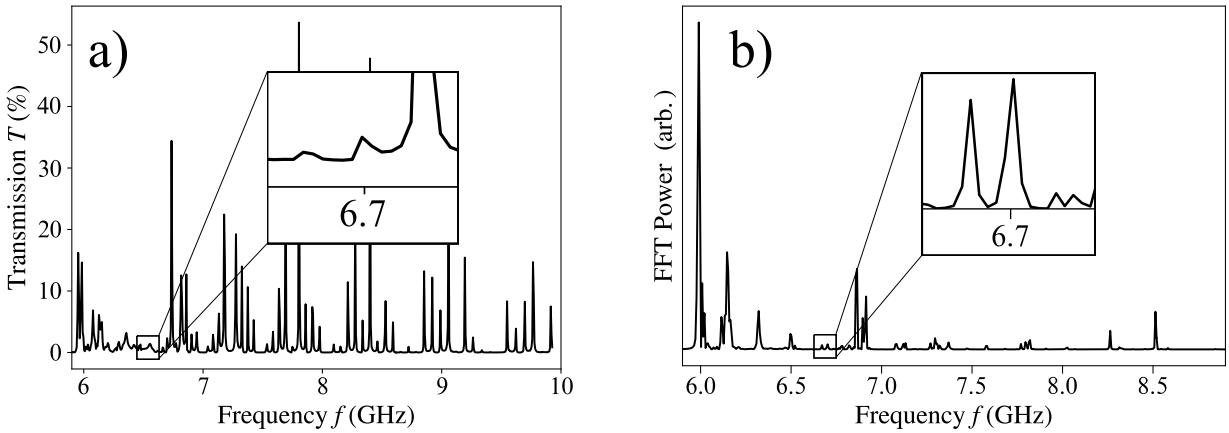

Figure 2. Spin-wave propagation behavior. *(a) Transmission behavior from input waveguide to ring. (b) Spin wave intensities in output waveguide. The frequency to excite the neuron with was required to have 0%, or close to 0%, transmission, non-zero FFT Power, and be well above ferromagnetic resonance (FMR), determined by plotting frequency f as a function of wavenumber k and found to be around 6.0 GHz. The excitation frequency of the neuron was determined to be 6.7 GHz.*

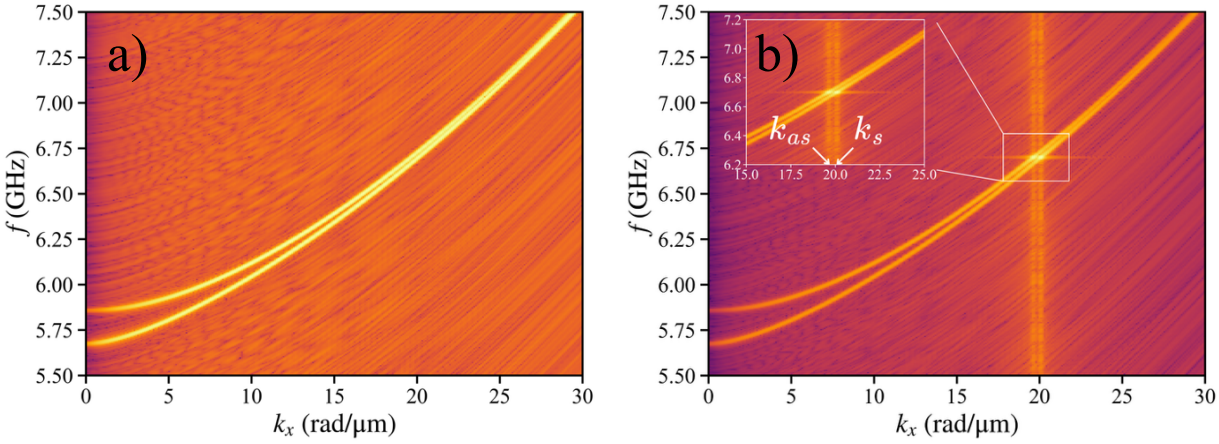

Figure 3. 2D spatiotemporal spectral maps demonstrating* k*-independent nonlinearity arising from parallel symmetric and antisymmetric modes*. Color indicates the logarithm of spectral intensity (arb. units). (a) Spectral map of a sinc-pulse excitation with waveguide separation Δ = 50 nm. (b) Spectral map of propagating spin waves with fixed frequency 6.7 GHz at low power (b_0 = 1 mT), with symmetric and antisymmetric spin-wave modes marked out. The resulting nearly parallel symmetric and antisymmetric dispersion curves at 6.7GHz enables robust nonlinear operation.*

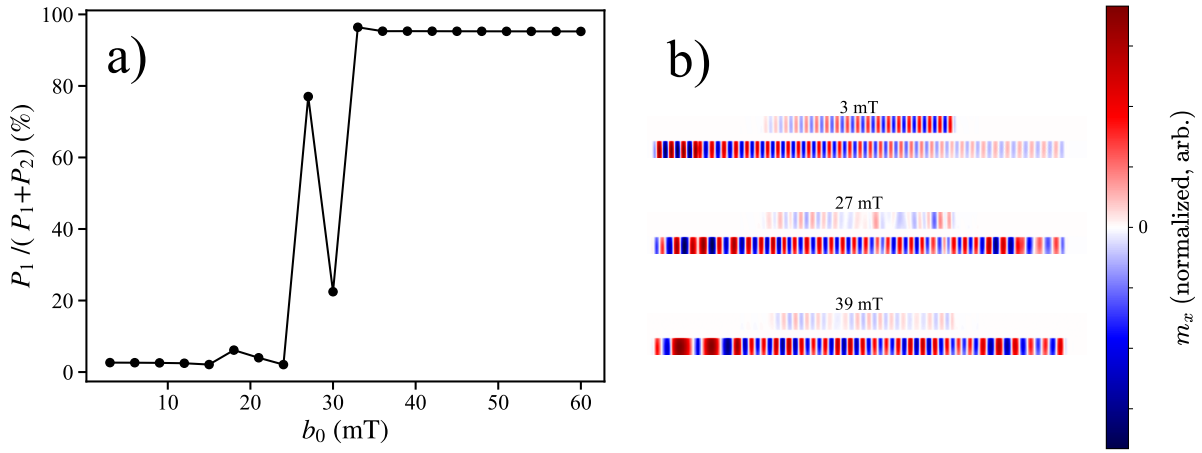

Figure 4. Nonlinear spin-wave routing in the directional coupler at 6.7 GHz. *(a) Percentage of spin waves remaining in the excitation waveguide as a function of input excitation field strength, b_0, with a sharp transition between 26 mT and 33 mT. (b) Spin-wave routing at b_0 = 3 mT, 27 mT and 39 mT, demonstrating near-complete energy transfer at low excitation and decoupling above the nonlinear threshold.*

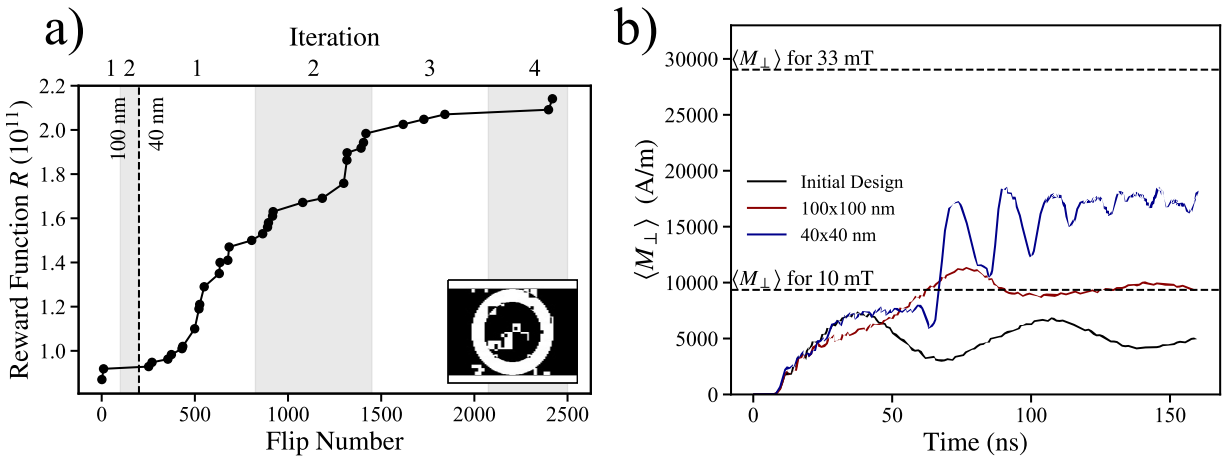

Figure 5. Progression of DBS algorithm. *(a) Improvements in output score of DBS across iterations, with best-case resonator geometry located at the bottom right. (b) Improvements in area-averaged, best-case output amplitude $\langle M_\perp \rangle$ immediately after the resonator across iterations. Notably, DBS has improved output amplitude to be greater than input amplitude but still falls short of the required amplitude for the neuron to 'fire'.*

DISCUSSION

The results demonstrate a proof-of-concept implementation of the integration and leak components of a LIF neuron, as well as a nonlinear activation mechanism. However, fully self-contained firing remains challenging, due to energy accumulation limits in nanoscale magnonic structures.

Functional Integration and Algorithmic Success

The primary success of this design lies in the implementation of the ring resonator as an integration node. The DBS optimization was crucial in improving steady-state output amplitude $\langle M_\perp \rangle$, that

exceeded baseline input excitation level. This is a critical milestone in confirming that inverse-design can overcome intrinsic magnetic damping to achieve a net gain in signal output power through spatial optimization — effectively implementing the 'thresholding' function of a neuron.

Analysis of Firing Threshold Gap

Despite the vast improvements made by DBS through inverse design, the peak amplitude remained below the critical threshold required to trigger the non-linear directional coupler. This current shortfall can be attributed to the high energy barrier required to reach this non-linear regime. The high damping constant (α) inherent to the simulated thin-film YIG acts as a continuous drain on the system's energy. Furthermore, the search space for optimization is computationally and time intensive. It was likely that the global maximum for energy accumulation was not reached within a reasonable timeframe, suggesting that with more intensive computational resources, different optimization strategies or a higher Q-factor resonator, the firing threshold could be met.

A higher input power could also improve output power. However, this is restricted to the linear regime, which 10 mT safely lies in. When a higher input power is used, it risks operating in the nonlinear regime, which may cause decoupling effects that shifts operating frequency which affects energy buildup. Therefore, device geometry must be optimized with nonlinear-aware algorithms that can compensate for such effects.

Fabrication Feasibility and Sensitivity

The optimized geometry features a minimum separation of 5 nm between the ring resonator and the waveguides. Although this small gap enhances coupling efficiency, it presents significant fabrication challenges due to lithographic resolution limits and edge roughness in nanofabrication processes [17] that could degrade interference patterns [18]. Experimental realization may therefore require design modifications that trade off coupling strength for improved manufacturability through increasing the gap or potentially compensating for losses through materials with lower damping such as Liquid Phase Epitaxy (LPE) grown YIG [12].

CONCLUSION AND FUTURE WORK

This study validates that inverse-designed magnonic structures can emulate the complex, time-dependent behavior of biological Leaky Integrate-and-Fire (LIF) neurons, crucial in implementing neuromorphic hardware. At the same time, the use of spin waves offers a potential energy efficiency gains over CMOS-based LIF neurons, as integration occurs through passive wave interference rather than the active charging of capacitors. Firing functionality has been shown through a nonlinear directional coupler structure, though to bridge the gap between integration and firing, ways to increase output power of the accumulator must be explored.

Cascading neurons must be further explored as well. If the output of one neuron can be successfully used to drive the input of another, this architecture could form the basis of a fully magnonic deep neural network operating at orders of magnitude less power than current electronic AI hardware.

CODE AVAILABILITY

All code used to run simulations is available in a GitHub repository located at https://github.com/SPMS01/Magnonic-Neuron.

DECLARATION OF GENERATIVE AI

Generative AI was used to aid in understanding unfamiliar Matplotlib functions and syntax.

BIBILOGRAPHY

[1] J. Backus, "Can programming be liberated from the von Neumann style? A functional style and its algebra of programs," *Commun. ACM*, vol. 21, no. 8, pp. 613–641, Aug. 1978, doi: 10.1145/359576.359579.

[2] E. García-Martín, C. F. Rodrigues, G. Riley, and H. Grahn, "Estimation of energy consumption in machine learning," *J. Parallel Distributed Comput.*, vol. 134, pp. 75–88, Aug. 2019, doi: 10.1016/j.jpdc.2019.07.007.

[3] D. Ham, H. Park, S. Hwang, and K. Kim, "Neuromorphic electronics based on copying and pasting the brain," *Nature Electronics*, vol. 4, no. 9, pp. 635–644, Sep. 2021, doi: 10.1038/s41928-021-00646-1.

[4] G. Indiveri and S.-C. Liu, "Memory and information processing in neuromorphic systems," *Proceedings of the IEEE*, vol. 103, no. 8, pp. 1379–1397, Aug. 2015, doi: 10.1109/JPROC.2015.2444094.

[5] A. V. Chumak, V. I. Vasyuchka, A. A. Serga, and B. Hillebrands, "Magnon spintronics," *Nature Physics*, vol. 11, pp. 453–461, Jun. 2015, doi: 10.1038/nphys3347.

[6] V. V. Kruglyak, S. O. Demokritov, and D. Grundler, "Magnonics," *Journal of Physics D: Applied Physics*, vol. 43, no. 26, p. 264001, Jun. 2010, doi: 10.1088/0022-3727/43/26/264001.

[7] L. J. Cornelissen, J. Liu, R. A. Duine, J. Ben Youssef, and B. J. van Wees, "Long-distance transport of magnon spin information in a magnetic insulator at room temperature," *Nature Physics*, vol. 11, pp. 1022–1026, Sep. 2015, doi: 10.1038/nphys3465.

[8] S. Choi, K. S. Lee, and S. K. Kim, "Spin-wave interference," *Applied Physics Letters*, vol. 89, no. 6, Art. no. 062501, 2006, doi: 10.1063/1.2259813.

[9] L. F. Abbott, "Lapicque's introduction of the integrate-and-fire model neuron (1907)," *Brain Res. Bull.*, vol. 50, nos. 5–6, pp. 303–304, 1999, doi: 10.1016/S0361-9230(99)00161-6.

[10] X. Ge, R. Verba, P. Pirro, A. V. Chumak, and Q. Wang, "Deeply nonlinear magnonic directional coupler," *Nano Lett.*, vol. 25, no. 36, pp. 13490–13495, Sep. 2025, doi: 10.1021/acs.nanolett.5c02758.

[11] A. Vansteenkiste, J. Leliaert, M. Dvornik, M. Helsen, F. Garcia-Sanchez, and B. Van Waeyenberge, "The design and verification of Mumax3," *AIP Advances*, vol. 4, no. 10, Art. no. 107133, Oct. 2014, doi: 10.1063/1.4899186.

[12] C. Dubs, O. Surzhenko, R. Thomas, J. Osten, T. Schneider, K. Lenz, J. Grenzer, R. Hübner, and E. Wendler, "Low damping and microstructural perfection of sub-40 nm-thin yttrium iron garnet films grown by liquid phase epitaxy," *Phys. Rev. Mater.*, vol. 4, no. 2, p. 024416, Feb. 2020, doi: 10.1103/PhysRevMaterials.4.024416.

[13] Q. Wang, A. Hamadeh, R. Verba, "A nonlinear magnonic nano-ring resonator," *npj Computational Materials*, vol. 6, no. 1, Dec. 2020, doi: 10.1038/s41524-020-00465-6.

[14] Q. Wang, A. V. Chumak, and P. Pirro, "Inverse-design magnonic devices," *Nature Commun.*, vol. 12, no. 1, p. 2636, May 2021, doi: 10.1038/s41467-021-22897-4.

[15] Z. Chen, G. J. Lim, C. C. I. Ang, T. Jin, F. Tan, B. W. H. Cheng, and W. S. Lew, "Voltage-controlled half adder via magnonic inverse design," *Appl. Phys. Lett.*, vol. 126, no. 13, p. 132406, Mar. 2025, doi: 10.1063/5.0256599.

[16] F. Li, D. Li, C. Wang et al., "An artificial visual neuron with multiplexed rate and time-to-first-spike coding," *Nat. Commun*., vol. 15, p. 3689, May 2024, doi: 10.1038/s41467-024-48103-9.

[17] V. R. Manfrinato, L. Zhang, D. Su, H. Duan, R. G. Hobbs, E. A. Stach, and K. K. Berggren, "Resolution limits of electron-beam lithography toward the atomic scale," *Nano Lett.*, vol. 13, no. 4, pp. 1555–1558, Apr. 2013, doi: 10.1021/nl304715p.

[18] T. Yu, S. Sharma, Y. M. Blanter, and G. E. W. Bauer, "Surface dynamics of rough magnetic films," *Phys. Rev. B*, vol. 99, no. 17, p. 174402, May 2019, doi: 10.1103/PhysRevB.99.174402.